Terahertz carrier dynamics in $SrTiO_3/LaTiO_3$ interfacial two-dimensional electron gases

Ahana Bhattacharya,[1] Andri Darmawan,[1,2] Jeong Woo Han,[1,3] Frederik Steinkamp,[1] Nicholas S. Bingham,[4,5,6] Ryan J. Suess,[1] Stephan Winnerl,[7] Markus E. Gruner,[1,2] Eric N. Jin,[6] Frederick J. Walker,[6] Charles H. Ahn,[6] Rossitza Pentcheva,[1,2] and Martin Mittendorff[1,2,*]

[1]*Universität Duisburg-Essen, Fakultät für Physik, 47057 Duisburg, Germany*
[2]*Universität Duisburg-Essen, Center for Nanointegration (CENIDE), 47057 Duisburg, Germany*
[3]*Chonnam National University, Department of Physics Education, Gwangju 61186, South Korea*
[4]*University of Maine, Department of Physics and Astronomy, Orono, Maine 04469, USA*
[5]*University of Maine, Frontier Institute for Research in Sensor Technologies, Orono, Maine 04469, USA*
[6]*Yale University, Department of Applied Physics, New Haven, Connecticut 06511, USA*
[7]*Helmholtz-Zentrum Dresden-Rossendorf, Bautzner Landstraße 400, 01328 Dresden, Germany*

(Received 28 March 2025; revised 2 October 2025; accepted 6 October 2025; published 27 October 2025)

A two-dimensional electron gas (2DEG) forms at the interface of complex oxides like $SrTiO_3$ (STO) and $LaTiO_3$ (LTO), despite each material having a low native conductivity, as a band and a Mott insulator, respectively. The interface 2DEG hosts charge carriers with moderate charge carrier density and mobility that raised interest as a material system for applications like field-effect transistors or detectors. Of particular interest is the integration of these oxide systems in silicon technology. To this end we study the carrier dynamics in a STO/LTO/STO heterostructure epitaxially grown on Si(001) both experimentally and theoretically. Linear THz spectroscopy was performed to analyze the temperature dependent charge carrier density and mobility, which was found to be in the range of 10^{12} cm^{-2} and 1000 cm^2 V^{-1} s^{-1}, respectively. Pump-probe measurements revealed a very minor optical nonlinearity caused by hot carriers with a relaxation time of several 10 ps, even at low temperature. Density functional theory calculations with a Hubbard U term on ultrathin STO-capped LTO films on STO/Si(001) show an effective mass of 0.64–0.68 m_e.

DOI: 10.1103/g23p-b4m5

I. INTRODUCTION

Heterostructures of complex transition metal oxides feature interface phenomena that are distinct from the bulk ranging from the formation of two-dimensional electron gases (2DEGs) to superconductivity or magnetism [1–5]. The 2DEGs originate from a discontinuity in the polarity of the crystal structure at the atomically sharp interfaces [6]. Depending on the composition of the oxide heterostructures, the 2DEG can host charge carriers with high mobility and high carrier density [7]. Electrostatic gating enables control over the charge carrier density, thus making it a feasible option for devices like field-effect transistors or detectors [8–11]. As it was recently shown, the 2DEG in heterostructures of the band insulator STO and the Mott insulator LTO epitaxially grown on Si(001) features a high carrier density of about 10^{12} cm^{-2}, with a mobility in the range of 100 cm^2 V^{-1} s^{-1} at room temperature, making it particularly interesting for devices [12].

While the dc conductivity has been studied extensively for such structures, there are relatively few studies investigating the THz conductivity [13,14]. In contrast to dc measurements, THz spectroscopy allows optical access to the free charge carriers without the need for electrical contacts [15]. Furthermore, 2DEGs allow the application of a thin film model, which directly gives access to the complex conductivity as a function of the frequency. In case the 2DEG is characterized by a THz conductivity that follows the Drude model, the carrier density and mobility can be directly derived from the measured results [15].

Beyond the complex conductivity, pump-probe experiments give insight into the nonequilibrium charge carrier dynamics, which is of key importance for applications and the development of devices [16]. For this, the sample is excited by a strong optical pulse, followed by a much weaker pulse to probe the pump-induced changes of the transmission or reflection. Measuring the differential probe intensity as a function of the time delay between pump and probe pulses directly allows the observation of the charge carrier relaxation. In contrast to pump-probe experiments in the visible to near-infrared range, where usually interband excitation is the dominating excitation mechanism, the low photon energy in the THz range usually does not allow for direct interband excitation ($E_{\mathrm{phot}} \approx 4$ meV @ 1 THz). At the moderate fluence values applied in our experiments, multiphoton, i.e., field induced interband excitation, is negligible. This is

*Contact author: martin.mittendorff@uni-due.de

corroborated experimentally by the observed sublinear increase of the pump-probe signal. For the multiphoton interband excitation, a strongly superlinear increase of the pump-probe signals would be expected. As a result, intraband excitation, which can often well be described by the Drude model, leads to a nonequilibrium carrier distribution.

Here we study the nonequilibrium carrier dynamics of the 2DEG at the STO/LTO interface in the vicinity of the Si(001) substrate. Linear THz time-domain spectroscopy reveals the carrier density and mobility as a function of the temperature, while pump-probe experiments performed in the THz spectral range give insights into the relaxation dynamics of optically excited charge carriers. For the samples investigated in this study, we found a charge carrier density on the order of 10^{12} cm^{-2} and mobility in the range of 1000 cm^2 V^{-1} s^{-1}, the THz conductivity is well described by the Drude model. Intraband excitation with a fluence of about 200 nJ cm^{-2} leads to a rather small pump-induced increase in transmission of about 0.04%. The experimental results are complemented by density functional theory (DFT) calculations with an on-site Hubbard term to explore the electronic properties of the 2DEG. Our results show an effective mass of 0.64–0.68 m_e, with m_e being the electron rest mass. The calculated effective mass is used as input for simulations of the experimental results via a two-temperature model, which agrees qualitatively with the experimental findings.

II. EXPERIMENTAL METHODS AND RESULTS

The samples are grown by molecular beam epitaxy (MBE) on a low-doped and high resistive Si substrate. The heterostructures are comprised of 4.5 unit cells (uc) STO on Si, 2 uc LTO, and capped by 5 uc STO. Details of the sample growth can be found in Ref. [12], a sketch of the sample is shown in Fig. 1(a). A second sample of STO on Si, but without the intermediate 2 uc LTO layer, serves as reference for spectroscopic measurements. This way, we can exclude any contribution stemming from a 2DEG forming at the STO/Si interface or the STO/vacuum interface.

To characterize the charge carrier density and mobility as a function of the temperature, we performed THz time-domain spectroscopy (THz TDS). The measurements were performed in a closed-cycle cryostat equipped with z-cut quartz windows, enabling temperature dependent measurements in the temperature range from 5 K to room temperature.

The experimental transmission as a function of the frequency and the temperature is shown in Fig. 1(b); the oscillations of the transmission, appearing as ripples along the temperature axis, are caused by multiple reflections within the sample. Even though 2DEGs in STO are characterized by a rather complex interplay of electron-electron and electron-phonon scattering [17], the THz transmission can be well described with a simple Drude model. To extract the carrier density and mobility from the experimental results, we fit a Drude conductivity in combination with a thin film model to the experimental results via [18]

$$t(\omega) = \left| \frac{E_{\text{sample}}(\omega)}{E_{\text{reference}}(\omega)} \right| = \left| \frac{n_{Si} + 1}{n_{Si} + 1 + Z_0 \sigma(\omega)} \right|, \qquad (1)$$

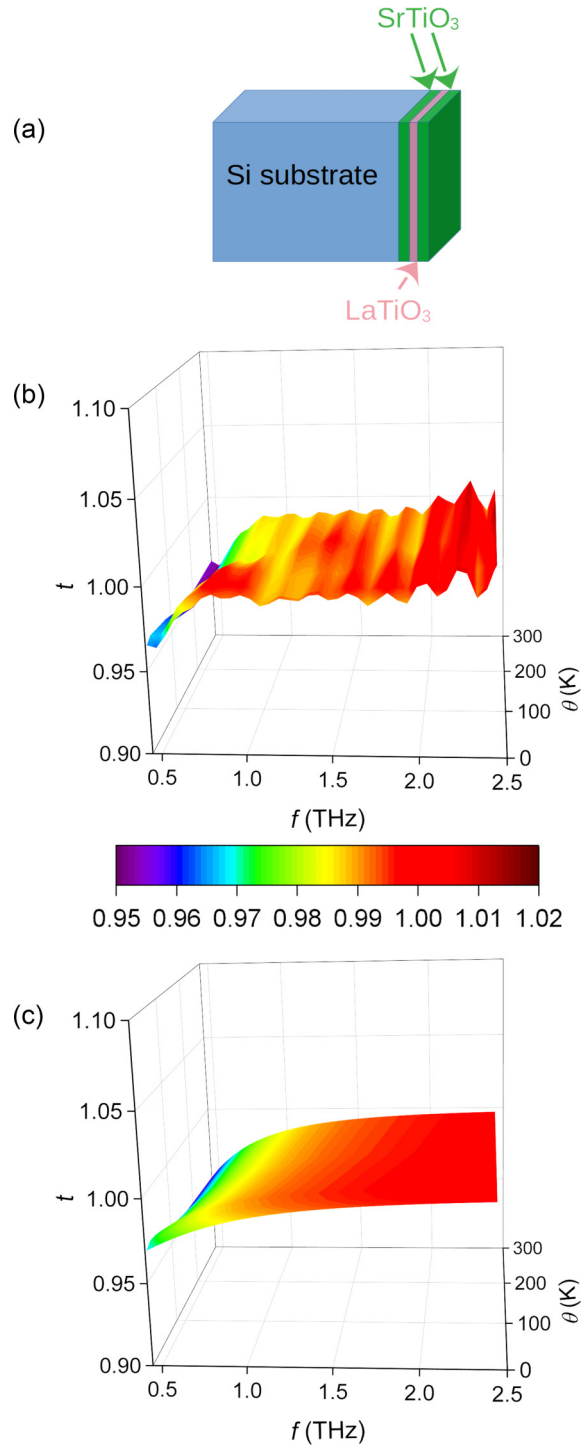

FIG. 1. (a) Sketch of the sample structure. Experimental (b) and fitted (c) THz field transmission (t) as a function of the frequency (f) and temperature (θ).

where $t(\omega)$ is the THz field transmission obtained from the sample and reference spectra $E_{\text{sample}}(\omega)$ and $E_{\text{reference}}(\omega)$, respectively. The refractive index of the substrate is represented by n_{Si}, Z_0 is the free-space impedance, and $\sigma(\omega)$ is the sheet conductivity of the 2DEG. The latter is derived from the Drude model via

$$\sigma(\omega) = \frac{ne^2\tau}{m^*(1 - i\omega\tau)}, \qquad (2)$$

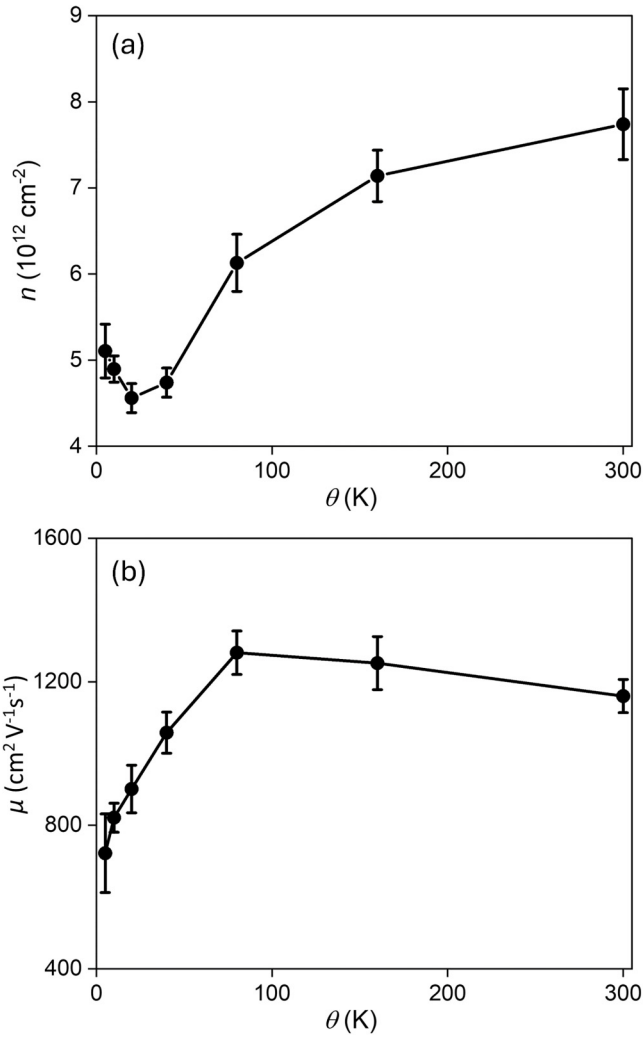

FIG. 2. Extracted (a) charge carrier density (n) and (b) mobility (μ) as a function of the temperature (θ).

where m^* represents the effective mass, τ the momentum scattering time, n is the sheet carrier density, and e the electric charge of an electron. The effective mass m^* is derived from the DFT simulations as described below. It is obtained by averaging over the calculated values of effective masses of the 2DEG along Γ-M and Γ-X directions [the band structure is depicted in Fig. 4(c)]. As a result, we get the charge carrier density and mobility as a function of the temperature via $\mu = \frac{e \cdot \tau}{m^*}$, as shown in Figs. 2(a) and 2(b), respectively.

The mobility is observed to increase moderately with temperature and reaches significantly above 1000 $cm^2\,V^{-1}\,s^{-1}$ before decreasing to about 1160 $cm^2\,V^{-1}\,s^{-1}$ at room temperature. The charge carrier density decreases slightly with temperature on heating the sample from 5 K to 20 K. On heating beyond 20 K, charge carrier density increases with temperature, reaching a value of approximately $7.7 \cdot 10^{12}\,cm^{-2}$ at room temperature, which is consistent with earlier findings [12]. The magnitude of the mobility and carrier density lies between those found for the two-carrier model (mobility of 10 000 $cm^2\,V^{-1}\,s^{-1}$ in the silicon and 100 $cm^2\,V^{-1}\,s^{-1}$ in the oxide layers) used in Ref. [12].

To measure the nonequilibrium carrier dynamics in the 2DEG, we performed pump-probe experiments at the free-electron laser (FEL) facility FELBE at Helmholtz-Zentrum Dresden-Rossendorf. To efficiently excite the 2DEG via free-carrier absorption and avoid heating via phonon absorption [19], we tuned the FEL to 1.35 THz, corresponding to a photon energy of about 5.6 meV. The FEL provides a continuous pulse train with a repetition rate of 13 MHz [20], a small fraction of about 2% of the FEL power is split off to serve as probe, the polarization is rotated by 90° after passing a delay stage. The majority of the FEL power is guided to a parabolic mirror, focusing both, pump and probe beam, on the sample. The pump beam is focused to a spot size of 800 × 800 μm^2 (FWHM) and blocked behind the sample, the probe beam is guided through an additional polarizer in order to minimize scattered pump radiation, before detection with a bolometer. The sample is mounted in a flow cryostat to maintain a sample temperature of 10 K. In order to avoid spurious pump-probe signals stemming from a potential 2DEG at the STO/ Si(001) interface and/or at the STO/vacuum interface, we performed measurements on the reference sample, observing no measurable change in transmission.

The experiments are performed at four different pump fluences of 16 $nJ\,cm^{-2}$, 53 $nJ\,cm^{-2}$, 106 $nJ\,cm^{-2}$, and 185 $nJ\,cm^{-2}$, the corresponding pump-probe signals are shown in Fig. 3(a). As can be seen, only a minor pump-induced change in transmission of about 0.04% is observed at the highest pump fluence. To measure these very small pump-induced changes in transmission, we averaged over 40 measurements at each fluence. After the peak of the pump-probe signal is reached, the signal decays on a time scale of about 50 ps, indicating a fast cooling of the hot carriers. The lines in Fig. 3(a) serve as a guide to the eye, indicating standard pump-probe signals that can be described by an error function for the rising edge and an exponential decay for the carrier relaxation. Due to the poor signal-to-noise ratio, the carrier relaxation time cannot be determined precisely. The maximum of the pump-probe signal scales with the square root of the pump fluence, which is represented by a phenomenological fit as a red solid line in Fig. 3(b).

III. THEORETICAL RESULTS AND DISCUSSION

Density functional theory calculations were performed on STO/LTO/STO/Si(001) as well as STO/Si(001) using the Vienna *ab initio* simulation package (VASP) [21–23] which implements the projector augmented wave (PAW) [24,25] method and pseudopotentials. The PBE [26] exchange-correlation functional within the generalized gradient approximation was used with an on-site Hubbard U term in the rotationally invariant formulation of Dudarev *et al.* [27]. $U_{\mathrm{eff}} = 5\,\mathrm{eV}$ and 8 eV are applied on the Ti *3d* and La *4f* states, respectively, consistent with previous work [28,29]. We employed a $p(2 \times 2)$ lateral unit cell consisting of four inequivalent Ti sites per layer in order to allow octahedral tilts and rotations, as well as an antiferromagnetic G-type ordering for the bulk LTO phase. The lateral lattice constant is fixed to the experimental lattice constant of Si (5.43 Å) exposing the STO and LTO films to −1.70% and −4.04% compressive strain, respectively. Asymmetric slabs were utilized with a

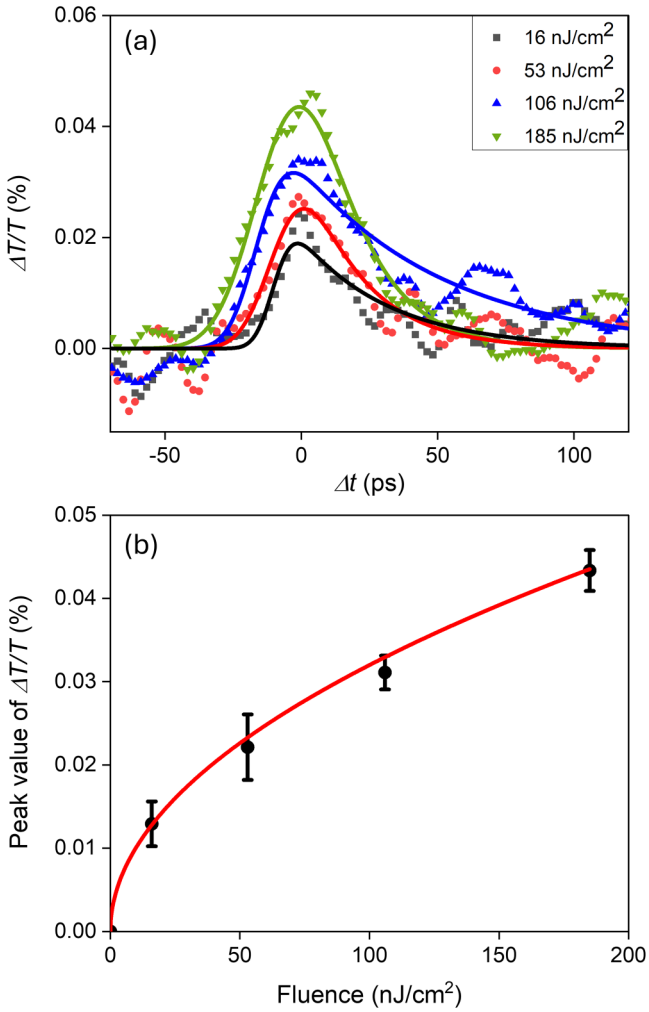

FIG. 3. Pump-induced change in transmission (ΔT/T) as a function of the delay time (Δt) for various pump fluences. The solid lines serve as guides to the eye. (b) Maximum pump-induced change in transmission as a function of the applied pump fluence, the red line represents a phenomenological square root fit.

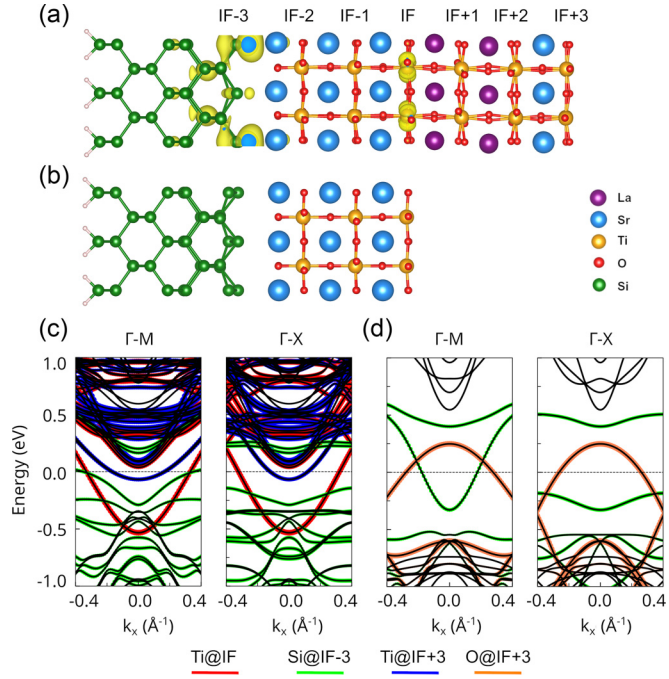

FIG. 4. Spin density of (a) STO/LTO/STO on reconstructed Si(001) and (b) STO on reconstructed Si(001), integrated between −0.6 eV and the Fermi energy $E_F = 0$ with isosurface value of 0.0006 e/ Å^3). The lower panels show the site-resolved band structure along the Γ-M and Γ-X directions in (c) STO/LTO/STO/Si(001) and (d) STO/Si(001).

1ML STO capping layer, followed by 2MLs of LTO and 3MLs of STO on 9 MLs reconstructed Si(001) substrate, whose bottom side is passivated by H. A vacuum region of 30 Å is added to avoid interactions between the slab and its periodic images. Additionally, we have considered 3ML STO/Si(001) as a reference system. We model the interface between STO and Si(001) [30] by a SrO termination at the reconstructed Si(001) interface, as previously reported by Chen *et al.* [31]. Overall, the studied systems contain 164 and 104 atoms for STO/LTO/STO/Si(001) and STO/Si(001), respectively. To confirm the effective masses for the 2DEG, we performed additional calculations with 3ML LTO on top of 3ML STO/Si (001) without STO capping, as well as 3ML of LTO on top of 5ML STO without considering the Si substrate. In the latter case, the lateral lattice parameters were constrained to the ones of STO or Si, to disentangle the effect of strain and the role of the Si substrate. We used an energy cutoff of 500 eV and sampled the Brillouin zone using a 5 × 5 × 1 Γ-centered k mesh. The ionic positions were fully relaxed.

Figures 4(a) and 4(b) display side views of the relaxed systems. For STO/LTO/STO/Si(001) the spin-density, integrated from −0.6 eV to E_F, displays a significant contribution at the LTO/STO interface with d_{xy} orbital polarization at the Ti sites as well as at the topmost Si layers. The band structure shown in Fig. 4(c) indicates that several conduction bands cross the Fermi level and thus contribute to the metallicity of the system and the formation of a 2DEG. The main contribution arises from Ti *3d* states at the LTO/STO interface with some participation of Si at the STO/Si(001) interface (IF-3). In the presence of a Si substrate, the carriers at the LTO/STO interface have mainly d_{xy} character, whereas the d_{xz} and d_{yz} orbitals are lying above the Fermi level. On the other hand, for LTO/STO(001) without a Si substrate, the carriers involved in the formation of the 2DEG have an additional d_{xz}, d_{yz} contribution [32], independent of potential strain in the layer (cf. Appendix C).

Furthermore, we have calculated the effective mass of the bands at the LTO/STO interface contributing to the 2DEG along the Γ-M and Γ-X directions from the band structure depicted in Fig. 4(c). The calculated effective mass along the Γ-M direction is 0.64 m_e while along the Γ-X direction is 0.68 m_e. Those bands are stemming from the $3d_{xy}$ orbitals of Ti at the LTO/STO interface. In contrast, the reference system shows only two bands crossing at E_F, a hole band contributed by O at the surface (IF+3), as well as an electron band of Si at the interface (IF-3) as seen in Fig. 4(d). Our results show that the 2DEG at the LTO/STO interface has predominantly Ti d_{xy} character. Note that, due to the high numerical cost, the

simulated heterostructure has less layers of the constituents compared to experiment. To ensure that there is no significant dependence of the effective masses on the layer thickness, we have performed calculations for two LTO thicknesses with and without $SrTiO_3$ capping layers and obtain consistently effective masses in the range 0.63–0.68 m_e.

To simulate the dynamics of the 2DEG, we perform calculations based on a two-temperature model via

$$\alpha_e \theta \frac{d\theta}{dt} + \beta(\theta - \theta_l) = A(\theta) I(t), \tag{3}$$

where α_e represents the specific heat of the 2DEG, which can be derived from the effective mass, assuming a parabolic dispersion relation. The temperature of the 2DEG and the lattice are represented by θ and θ_l, respectively. $\beta = 1.4 \cdot 10^4\,\mathrm{Wm^{-2}K^{-1}}$ is a fit parameter for the carrier relaxation time, $A(\theta)$ is the absorption of the 2DEG derived from the thin film model at the photon frequency applied in the experiment (1.35 THz), and $I(t)$ describes the temporal evolution of the pump pulse. The temperature dependent parameters for the absorption, i.e., the carrier density and mobility, are interpolated from the THz TDS results shown in Fig. 2. From the temporal evolution of the electron temperature, we calculated the pump-induced change in transmission via the thin-film model shown in Fig. 5(a); Fig. 5(b) shows the maximum change in transmission as a function of the pump fluence. While the theoretical results qualitatively reproduce the experimental results including the fluence dependence, the absolute values are about five times higher than experimentally observed. From the specific heat mentioned above, we estimate a maximum increase of the electron temperature of about 18 K. We note that the quantitative deviation between the two-temperature model and the experimental results is likely related to the fundamental difference between the pump-probe experiments and the THz TDS measurements: while the THz TDS measurements were taken at equilibrium, i.e., both electrons and lattice have the same temperature, the pump-probe measurements probe a hot carrier distribution in a cold lattice.

The pump-induced change in transmission is rather small compared to other 2DEGs based on conventional heterostructures [33,34]. Based on the results of the thin film model, we attribute the remarkably small pump-probe signals to the temperature dependence of the Drude conductivity, and thereby the charge carrier density and mobility, of the oxide-interface 2DEG in our STO/LTO heterostructure. In the interfacial 2DEGs studied here, we see the carrier density initially decreases with increasing temperature at first and reaches a minimum value at 20 K. Only for temperatures above this minimum value is an increase in carrier density observed [cf. Fig. 2(a)]. The mobility in the STO/LTO 2DEG increases until a temperature of about 80 K beyond which it shows a small drop, indicating weak electron-phonon scattering. The decrease in mobility below 80 K as well as the initial decrease of carrier density with temperature point toward the presence of ionized impurities at the interface. The trends observed in the carrier density and mobility in the STO/LTO 2DEG are both resulting in a pump-induced increase in transmission. To identify the impact of both contributions, we performed additional calculations keeping one of the parameters fixed and only varying the second one. With this, we found that the impact of the carrier mobility and the carrier density are nearly equal, reaching 0.14% and 0.11% at highest fluence, respectively. Other effects like phonon absorption or the temperature dependence of the optical properties of the substrate can be excluded, as the pump-probe measurements on the reference without LTO layer did not show measurable pump-probe signals (cf. Appendix B).

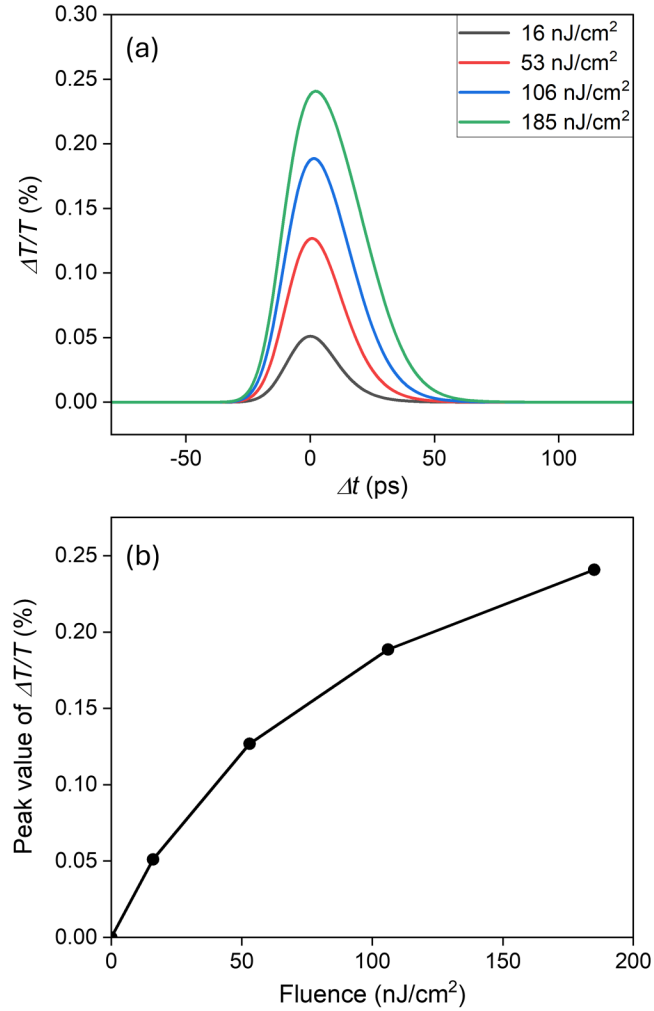

FIG. 5. (a) Simulated pump-induced change in transmission (ΔT/T) derived from a two-temperature model. (b) Simulated maximum of the pump-induced change in transmission as a function of the applied pump fluence.

IV. SUMMARY

In conclusion, we investigated the physical properties of the 2DEG formed at the STO/LTO interface via THz TDS and high intensity THz pump-probe measurements. The experiments are complemented by DFT+U calculations of the 2DEG that find an effective mass of 0.64–0.68 m_e. The optical properties and the dynamical evolution of the 2DEG are modeled via a thin-film model and a two-temperature model, respectively. We found a surprisingly low impact of the intraband excitation on the sample conductivity, that resulted in small pump-induced changes of the transmission that were less than 0.05%.

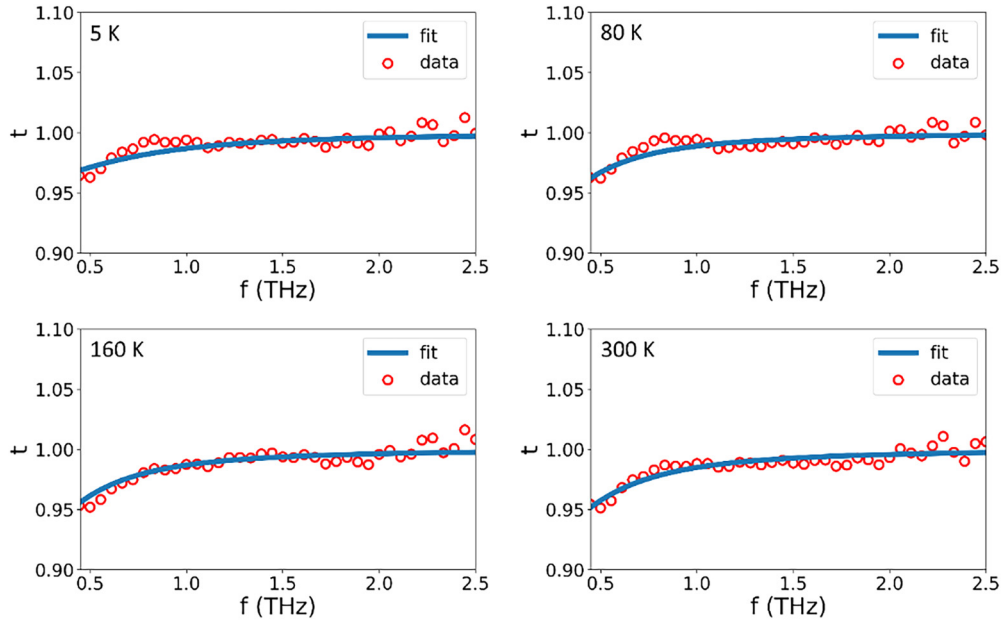

FIG. 6. Measured THz field transmission (red open circles) and the according Drude fits (blue solid lines) at 5 K, 80 K, 160 K, and 300 K.

ACKNOWLEDGMENTS

This study was funded by the Deutsche Forschungsgemeinschaft (DFG, German Research Foundation)—Project ID 278162697—SFB1242. We thank J. Michael Klopf and the ELBE team for their assistance. Work at Yale was supported by the Office of Naval Research Multidisciplinary University Research Initiative to support the EXtreme Electron DEvices (EXEDE) program (synthesis and characterization) and by NSF DMR-2412358 (analysis). We acknowledge computational time at the Leibniz Rechenzentrum, project pr87ro and the supercomputer MagnitUDE.

DATA AVAILABILITY

The data that support the findings of this article are not publicly available upon publication because it is not technically feasible and/or the cost of preparing, depositing, and hosting the data would be prohibitive within the terms of this research project. The data are available from the authors upon reasonable request.

APPENDIX A: THZ TDS ANALYSIS

For better visibility of the fit to the THz TDS results, we provide four exemplary 2D plots for the transmission at temperatures of 5 K, 80 K, 160 K, and 300 K, as shown in Fig. 6. The red circles represent the experimental results, and the blue

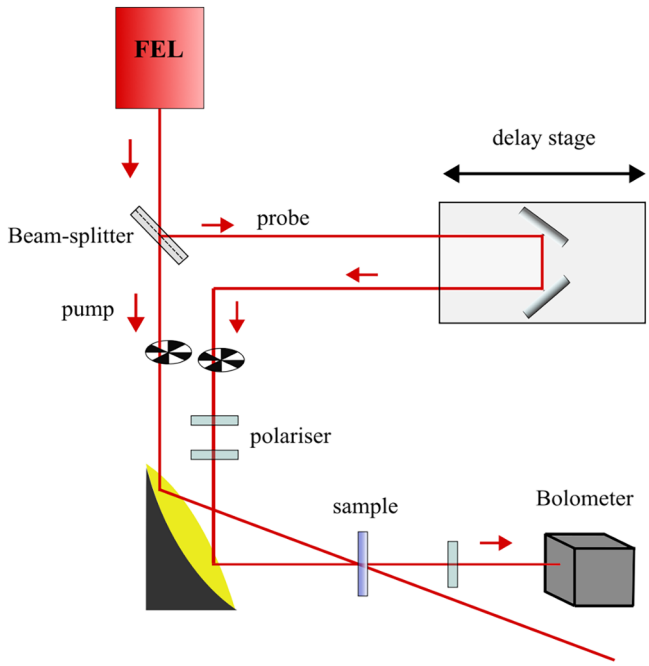

FIG. 7. Sketch of the pump-probe setup.

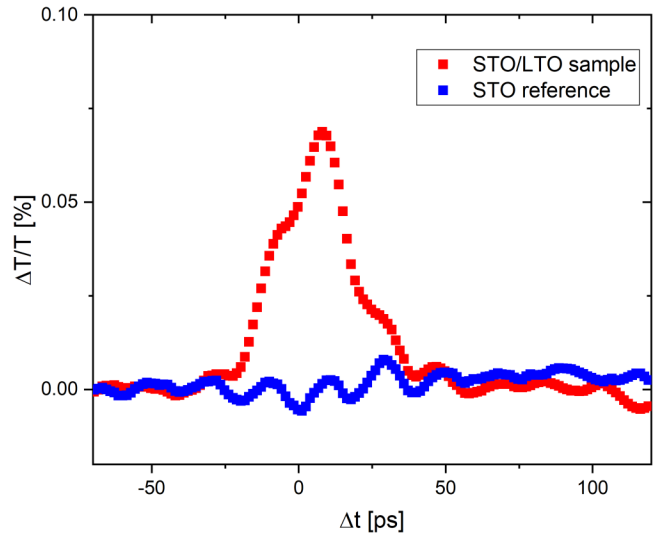

FIG. 8. Pump-probe signals of the STO/LTO sample and the reference without the LTO layer, measured at a fluence of 280 nJ cm^{-2} at a frequency of 1.5 THz.

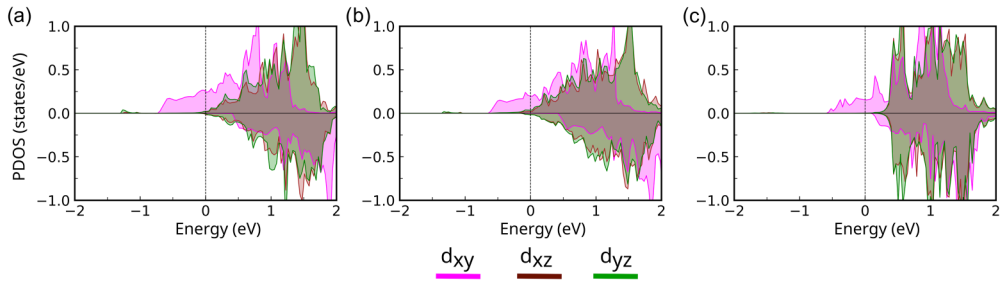

FIG. 9. Orbitally projected DOS of Ti at the interface showing the occupation of t_{2g} states of the system without Si(001) (a) strained to a_{STO}, (b) strained to a_{Si} and with (c) Si(001).

line corresponds to the Drude fit at the given temperature. The Drude conductivity as a function of the carrier density and mobility is given by Eq. (2), which is implemented into the thin film model in Eq. (1), which describes the transmission as a function of the Drude conductivity. With this combination, we get the transmission as a function of the frequency, the fit parameters are the carrier density and mobility. All other parameters (e.g., the effective mass) are fixed to the described values.

APPENDIX B: THZ PUMP-PROBE EXPERIMENTS

A sketch of the pump-probe setup as described in the main text is provided in Fig. 7. The first polarizer in the probe beam is set to 45° with respect to the FEL polarization, the second one is set to 90° in order to reach cross polarization of the pump and probe beams. A polarizer in front of the bolometer blocks the scattered pump radiation to minimize background signals. The temporal resolution of the setup is determined by the FEL pulse duration, which is in the range of about 20 ps.

As briefly mentioned in the main text, a reference without LTO layer was measured to ensure that the observed pump-probe signals stem from the STO/LTO interface, not from the STO/Si or STO/vacuum interface. Sample and reference were mounted next to each other in the same cryostat, both measured under identical experimental conditions. Figure 8 shows the pump-probe signals of the STO/LTO sample as well as the reference sample without the LTO layer. Note that these measurements were done during an earlier measurement campaign at the free electron laser at a slightly higher frequency of about 1.5 THz, also the fluence of about 280 nJ cm^{-2} was higher compared to the pump-probe signals described in the main text, the sample was identical to the one used in the measurements described in the main manuscript.

APPENDIX C: ORBITALLY PROJECTED DOS

The corresponding projected density of states is shown in Fig. 8. In order to assess the influence of the Si substrate and epitaxial strain, we studied systems consisting of 3ML LTO and 5ML STO without the Si substrate. We have considered here two cases with the lateral lattice constant set to the one of STO or Si. While in all three cases the dominant contribution to the 2DEG is from the Ti d_{xy} states, for the cases without the Si substrate there is an additional small contribution from the d_{xz} and d_{yz} states. These states are shifted to higher energies in the presence of the Si substrate [cf. Fig. 9(c)]. The effect is independent of the applied epitaxial strain as shown in Figs. 9(a) and 9(b).

[1] J. Mannhart and D. G. Schlom, Oxide interfaces – an opportunity for electronics, Science **327**, 1607 (2010).

[2] H. Y. Hwang, Y. Iwasa, M. Kawasaki, B. Keimer, N. Nagaosa, and Y. Tokura, Emergent phenomena at oxide interfaces, Nat. Mater. **11**, 103 (2012).

[3] S. Stemmer and S. J. Allen, Two-dimensional electron gases at complex oxide interfaces, Annu. Rev. Mater. Res. **44**, 151 (2014).

[4] Y.-Y. Pai, A. Tylan-Tyler, P. Irvin, and J. Levy, Physics of $SrTiO_3$-based heterostrcutures and nanostructures: A review, Rep. Prog. Phys. **81**, 036503 (2018).

[5] M. Yang, J. Zhou Ariando, T. C. Asmara, P. Krüger, X. J. Yu, X. Wang, C. Sanchez-Hanke, Y. P. Feng, T. Venkatesan, and A. Rusydi, Direct observation of room-temperature stable magnetism in $LaAlO_3/SrTiO_3$ heterostructures, ACS Appl. Mater. Interfaces **10**, 9774 (2018).

[6] A. Ohtomo and H. Y. Hwang, A high-mobility electron gas at the $LaAlO_3/SrTiO_3$ heterointerface, Nature (London) **427**, 423 (2004).

[7] K. Yang, S. Nazir, M. Behtash, and J. Cheng, High-throughput design of two-dimensional electron gas systems based on polar/nonpolar perovskite oxide heterostructures, Sci. Rep. **6**, 34667 (2016).

[8] C. W. Schneider, S. Thiel, G. Hammerl, C. Richter, and J. Mannhart, Microlithography of electron gases formed at interfaces in oxide heterostructures, Appl. Phys. Lett. **89**, 122101 (2006).

[9] C. Cen, S. Thiel, J. Mannhart, and J. Levy, Oxide nanoelectronics on demand, Science **323**, 1026 (2009).

[10] D. F. Bogorin, C. W. Bark, H. W. Jang, C. Cen, C. M. Folkman, C.-B. Eom, and J. Levy, Nanoscale rectification at the $LaAlO_3/SrTiO_3$ interface, Appl. Phys. Lett. **97**, 013102 (2010).

[11] P. D. Eerkes, W. G. van der Wiel, and H. Hilgenkamp, Modulation of conductance and superconductivity by top-gating in $LaAlO_3/SrTiO_3$ 2-dimensional electron system, Appl. Phys. Lett. **103**, 201603 (2013).

[12] E. N. Jin, A. Kakekhani, S. Ismail-Beigi, C. H. Ahn, and F. J. Walker, Two-dimensional electron gas oxide

remote doping of Si(001), Phys. Rev. Mater. **2**, 115001 (2018).

[13] A. Dubroka, M. Rössle, K. W. Kim, V. K. Malik, L. Schlutz, S. Thiel, C. W. Schneider, J. Mannhart, G. Herranz, O. Copie, M. Bibes, A. Barthelemy, and C. Bernhard, Dynamical response and confinement of the electrons at the $LaAlO_3/SrTiO_3$ interface, Phys. Rev. Lett. **104**, 156807 (2010).

[14] X. Liu, J. Zhang, Z. Zhang, X. Lin, Y. Yu, X. Xing, Z. Jin, Z. Cheng, and G. Ma, Thermodynamics of quasi-2D electron gas at BFO/Si interface probed with THz time-domain spectroscopy, Appl. Phys. Lett. **111**, 152906 (2017).

[15] S. Mitra, L. Avazpour, and I. Knezevic, Terahertz conductivity of two-dimensional materials: A review, J. Phys.: Condens. Matter **37**, 133005 (2025).

[16] T. Dong, S.-J. Zhang, and N.-L. Wang, Recent development of ultrafast optical characterizations for quantum materials, Adv. Mater. **35**, 2110068 (2023).

[17] P. D. C. King, S. McKeown Walker, A. Tamai, A. ke la Torre, T. Eknapakul, P. Buaphet, S.-K. Mo, W. Meevasana, M. S. Bahramy, and F. Baumberger, Quasiparticle dynamics and spin-orbital texture of the $SrTiO_3$ two-dimensional electron gas, Nat. Commun. **5**, 3414 (2014).

[18] J. Lloyd-Hughes and T.-I. Jeon, A review of the terahertz conductivity of bulk and nano-materials, J. Infrared Milli. Terahz. Waves **33**, 871 (2012).

[19] D. Nuzhnyy, J. Petzelt, S. Kamba, T. Yamada, M. Tyunina, A. K. Tagantsev, J. Levoska, and N. Setter, Polar phonons in some compressively stressed epitaxial and polycrystalline $SrTiO_3$ thin films, J. Electroceram. **22**, 297 (2009).

[20] M. Helm, S. Winnerl, A. Pashkin, J. M. Klopf, J.-C. Deinert, S. Kovalev, P. Evtushenko, U. Lehnert, R. Xiang, A. Arnold, A. Wagner, S. M. Schmidt, U. Schramm, T. Cowan, and P. Michel, The ELBE infrared and THz facility at Helmholtz-Zentrum Dresden-Rossendorf, Eur. Phys. J. Plus **138**, 158 (2023).

[21] G. Kresse and J. Hafner, *Ab initio* molecular dynamics for liquid metals, Phys. Rev. B **47**, 558 (1993).

[22] G. Kresse and J. Furthmüller, Efficiency of *ab-initio* total energy calculations for metals and semiconductors using a plane-wave basis set, Comput. Mater. Sci. **6**, 15 (1996).

[23] G. Kresse and J. Furthmüller, Efficient iterative schemes for *ab initio* total-energy calculations using a plane wave basis set, Phys. Rev. B **54**, 11169 (1996).

[24] P. E. Blöchl, Projector augmented-wave method, Phys. Rev. B **50**, 17953 (1994).

[25] G. Kresse and D. Joubert, From ultrasoft pseudopotentials to the projector augmented-wave method, Phys. Rev. B **59**, 1758 (1999).

[26] P. Perdew, K. Burke, and M. Ernzerhof, Generalized gradient approximation made simple, Phys. Rev. Lett. **77**, 3865 (1996).

[27] S. L. Dudarev, G. A. Botton, S. Y. Savrasov, C. J. Humphreys, and A. P. Sutton, Electron-energy-loss spectra and the structural stability of nickel oxide: An LADA+ U study, Phys. Rev. B **57**, 1505 (1998).

[28] S. Okamoto, A. J. Millis, and N. A. Spaldin, Lattice relaxation in oxide heterostructures: $LaTiO_3/SrTiO_3$ superlattices, Phys. Rev. Lett. **97**, 056802 (2006).

[29] D. Doennig, W. E. Pickett, and R. Pentcheva, Massive symmetry breaking in $LaAlO_3/SrTiO_3(111)$ quantum Wells: A three-orbital strongly correlated generalization of graphene, Phys. Rev. Lett. **111**, 126804 (2013).

[30] A. M. Kolpak, F. J. Walker, J. W. Reiner, Y. Segal, D. Su, M. S. Sawicki, C. C. Braodbridge, Z. Zhang, Y. Zhu, C. H. Ahn, and S. Ismail-Beigi, Interface-induced polarization and inhibition of ferroelectricity in epitaxial $SrTiO_3$/Si, Phys. Rev. Lett. **105**, 217601 (2010).

[31] T. Chen, K. Ahmadi-Majlan, Z. H. Lim, Z. Zhang, J. H. Ngai, and D. P. Kumah, Effect of buffer termination on intermixing and conductivity in $LaTiO_3/SrTiO_3$ heterostructures integrated on Si(110), J. Vac. Sci. Technol. A **40**, 013206 (2022).

[32] M. J. Veit, R. Arras, B. J. Ramshaw, R. Pentcheva, and Y. Suzuki, Nonzero Berry phase in quantum oscillations from giant Rashba-type spin splitting in $LaTiO_3/SrTiO_3$ heterostructures, Nat. Commun. **9**, 1458 (2018).

[33] J. R. Danielson, Y.-S. Lee, J. P. Prineas, J. T. Steiner, M. Kira, and S. W. Koch, Interaction of strong single-cycle terahertz pulses with semiconductor quantum wells, Phys. Rev. Lett. **99**, 237401 (2007).

[34] D. Sabbagh, J. Schmidt, S. Winnerl, M. Helm, L. Di Gaspare, M. De Seta, M. Virgilio, and M. Ortolani, Electron dynamics in silicon-germanium terahertz quantum fountain structures, ACS Photonics **3**, 403 (2016).